

Application of Large-Eddy Simulation to the Study of Pulsatile Flow in a Modeled Arterial Stenosis

R. Mittal

Assistant Professor.

S. P. Simmons

Graduate Student.

Department of Mechanical Engineering,
University of Florida,
Gainesville, FL 32611

H. S. Udaykumar

Assistant Professor.

Department of Mechanical Engineering,
University of Iowa,
Iowa City, IA 52242

The technique of large-eddy simulation (LES) has been applied to the study of pulsatile flow through a modeled arterial stenosis. A simple stenosis model has been used that consists of a one-sided 50 percent semicircular constriction in a planar channel. The inlet volume flux is varied sinusoidally in time in a manner similar to the laminar flow simulations of Tutty (1992). LES is used to compute flow at a peak Reynolds number of 2000 and a Strouhal number of 0.024. At this Reynolds number, the flow downstream of the stenosis transitions to turbulence and exhibits all the classic features of post-stenotic flow as described by Khalifa and Giddens (1981) and Lieber and Giddens (1990). These include the periodic shedding of shear layer vortices and transition to turbulence downstream of the stenosis. Computed frequency spectra indicate that the vortex shedding occurs at a distinct high frequency, and the potential implication of this for noninvasive diagnosis of arterial stenoses is discussed. A variety of statistics have been also extracted and a number of other physical features of the flow are described in order to demonstrate the usefulness of LES for the study of post-stenotic flows. [DOI: 10.1115/1.1385840]

Keywords: Turbulent Flows, Turbulence Modeling, Stenotic Flows, Cardiovascular Flows, Computational Fluid Dynamics, Hemodynamics, Bio-fluid Dynamics, Blood Flow

Introduction

Blood flow through arteries is inherently unsteady due to the cyclic nature of the heart pump, and Reynolds number can vary from $O(1)$ in the small arterioles to as high as $O(10^3)$ in the larger arteries. For instance, the peak Reynolds number in the ascending aorta of a dog has been measured to be approximately 4500, whereas that in the main pulmonary artery is about 3000 [1,2]. Although it is firmly established that steady laminar flow through a pipe becomes unstable at a Reynolds number (based on the mean velocity and pipe diameter) of about 2000 and fully turbulent flow ensues at about 4000 [3], flow pulsatility and the compliant nature of the arterial wall are expected to have a significant effect on the transition to turbulence in arterial flows [4,5]. In particular, the effect of pulsatility on transition to turbulence in arterial flows has been the subject of many previous studies and there is a significant amount of evidence that suggests that turbulence does occur in a wide variety of such flows [6,7].

The possibility of generating turbulence is greatly increased by the presence of a stenosis in the artery. For even moderate stenoses, the separated shear layer coming off the stenosis can become turbulent at a Reynolds number as low as a few hundred [8,9]. Turbulence can have a dramatic influence on the pressure drop and wall shear stress downstream of the stenosis, both of which can have a substantial negative influence on the cardiovascular system. For example, wall shear stresses and shear rates have been correlated with the incidence of atherosclerosis in the artery [10]. Turbulence downstream of the arterial stenosis is expected to alter the shear as well as pressure forces on the endothelium in the post-stenotic region. Furthermore, stress and pressure fields induced by the flow can also cause fracture of the plaque, which may further result in embolization and occlusion of arteries and arterial collapse [11]. The generation of turbulence

downstream of a stenosis also has important implications for diagnostic procedures. For instance, current procedures for locating severe stenosis includes detecting the murmurs (bruits) produced by the unsteady flow downstream of the stenosis [10,12,13]. Better understanding of the flow and turbulence in post-stenotic flow could possibly lead to more accurate diagnostic procedures in the future.

From the point of view of accurate computational modeling, such flows can be challenging. On the one hand the Reynolds number is high enough that direct numerical simulation (DNS), where all the spatial and temporal scales of turbulence are accurately resolved [14], would be extremely taxing on computing resources. On the other hand, both the pulsatile nature of the flow and the relatively low Reynolds number result in a flow that is far from fully developed turbulence. Consequently, conventional Reynolds-averaged Navier–Stokes (RANS) turbulence models [15], which are designed primarily for simulating well-developed, high-Reynolds-number turbulent flows are not well suited for these arterial flows.

Large-eddy simulation (LES) is an approach that can be considered to lie between DNS and RANS, and is, in our view, a technique well suited for the computational modeling of turbulent arterial flows. Unlike DNS, where all the spatial and temporal scales are resolved, in LES only the energy-containing scales (termed “large eddies”) of the turbulence are resolved spatially and temporally; the smaller scales, termed subgrid scales (SGS), are modeled [14]. The LES approach has a number of benefits over DNS and RANS. First, since the smallest scales do not need to be resolved, the spatial and temporal resolution required here can be substantially lower than that for a corresponding DNS. Secondly, unlike RANS modeling, LES provides time-accurate information about a wide range of dynamically important scales in the flow. It is therefore capable of providing better physical insight and has the potential to be a more accurate predictive tool. Finally, since the subgrid scales are in principal more universal in nature, relatively simple turbulence models can be employed for modeling these scales. Consequently, LES can be applied to a

Contributed by the Bioengineering Division for publication in the JOURNAL OF BIOMECHANICAL ENGINEERING. Manuscript received by the Bioengineering Division October 22, 2000; revised manuscript received March 26, 2001. Associate Editor: A. P. Yoganathan.

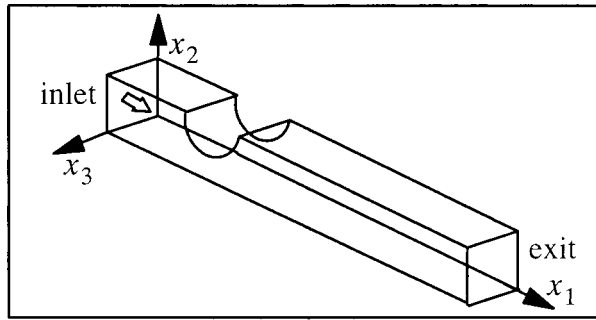


Fig. 1 Schematic of the stenosis model employed in the current simulations

wide range of turbulent flows without resorting to ad hoc “tuning” of the turbulence model to accommodate specific flow behavior [15]. The computational expense of these simulations typically increases with the Reynolds number and for relatively complex geometries, this has limited the application of LES to only moderately high Reynolds number turbulent flows. However, the Reynolds numbers of blood flow in the human cardiovascular system are limited to about $O(10^4)$ and this is well within the reach of present day computers.

In the current paper, the application of LES to a modeled arterial stenosis is described with the objective of demonstrating the utility of this technique for the analysis of turbulent and transitional cardiovascular flows. A wide variety of information can be extracted from a large-eddy simulation. This can then be used to gain a comprehensive understanding of the spatio-temporal dynamics of such flows. This is demonstrated here for the specific case of a modeled arterial stenosis.

Stenosis Model

A relatively simple model of a stenosed artery studied previously by Tutty [16] has been chosen in the current study. The geometry is shown in Fig. 1 and it consists of a planar channel with a one-sided semicircular stenosis. The stenosis reduces the channel area by 50 percent. However, unlike Tutty, who performed a two-dimensional simulation, in the current large-eddy simulation, allowance is made for periodic variation of flow quantities in the spanwise direction. It should be pointed out that turbulence is inherently a three-dimensional phenomenon and in keeping with this, LES is always carried out as a three-dimensional simulation. The diameter of the semicircular constriction is equal to the channel height, which is denoted by H . The channel extends $4H$ and $12H$ upstream and downstream of the center of the stenosis, respectively.

A parabolic inflow profile is imposed at the inlet and in a manner similar to Tutty [16], the flow rate per unit channel width is varied in a sinusoidal manner as $Q(t) = (Q_{\max}/2)[1 - \cos(2\pi t/T)]$ where T is the time period of the pulse and Q_{\max} is the maximum flow rate. The Strouhal number, which corresponds to the nondimensional frequency of the inlet flow oscillation, is defined as $St_0 = H^2/TQ_{\max}$ and the peak Reynolds number is defined as $Re = Q_{\max}/\nu$. The Womersley number is used widely in the description of cardiovascular flows and for this configuration, the Womersley number is given by $\alpha = (\pi Re St_0/2)^{1/2}$. At the exit, a convective boundary condition is applied that allows the vortex structures to exit the domain with minimal reflections. Periodic boundary conditions are applied on the spanwise boundaries and therefore, flow exiting from one spanwise boundary returns into the flow domain from the other spanwise boundary.

The flow downstream of an arterial stenosis is characterized by a separating, transitioning shear layer that evolves under the influence of a pulsatile inflow and interacts with the arterial walls downstream of the stenosis. The planar geometric model that has

been chosen here is relatively simple and obviously does not account for the circular arterial lumen. It does, however, include some of the important geometrical features of an arterial stenosis and is expected to exhibit many of the key features (as mentioned above) that characterize post-stenotic flow in a realistic artery. The simplicity of the chosen geometry reduces the computational expense of these simulations and allows us to obtain well-converged, accurate results, which are then analyzed in detail by extracting a variety of statistics.

Numerical Methodology

Detailed description of the LES methodology can be found in Rogallo and Moin [14], Germano et al. [17], and Lesieur and Metais [18]. In addition to this, the specific implementation of this technique and the numerical algorithm that is used here can be found in Mittal and Moin [19] and Kaltenbach et al. [20]. Here only a brief overview of the technique, as it is implemented in the current simulations, is provided.

Governing Equation and SGS Model. It has been well established that blood in the larger vessels can be modeled quite accurately as a Newtonian fluid [2,7] and therefore it is assumed that the flow through the modeled stenosis is governed by the unsteady, viscous, incompressible Navier–Stokes equations. The viewpoint taken in LES is that the velocity and pressure field can be decomposed as $u_i = \bar{u}_i + u'_i$ and $p = \bar{p} + p'$ where the bar denotes large scales that can be resolved on a given mesh and the prime quantities are the subgrid scales, i.e., the scales that are smaller than the mesh size and therefore cannot be resolved. The above-described decomposition can be applied to the incompressible Navier–Stokes equations and the following “filtered” equations obtained for the resolved scales:

$$\frac{\partial \bar{u}_i}{\partial x_i} = 0; \quad \frac{\partial \bar{u}_i}{\partial t} + \frac{\partial \bar{u}_i \bar{u}_j}{\partial x_j} = -\frac{\partial \bar{p}}{\partial x_i} + \frac{1}{Re} \frac{\partial^2 \bar{u}_i}{\partial x_j \partial x_j} - \frac{\partial \tau_{ij}}{\partial x_j} \quad (1)$$

where τ_{ij} is the subgrid scale tensor given by $\tau_{ij} = \overline{u_i u_j} - \bar{u}_i \bar{u}_j$. The subgrid scale tensor cannot be calculated directly in a simulation since it requires knowledge of u_i and therefore of u'_i , which is not known. Therefore, in order to close this system of equations, a model needs to be used for the subgrid scale tensor. The most widely used subgrid-scale stress model is an eddy viscosity type model where $\tau_{ij} - \delta_{ij}/3 \tau_{kk} = -2\nu_T \bar{S}_{ij}$. In this model, ν_T is the eddy viscosity and $\bar{S}_{ij} = 1/2(\partial \bar{u}_i / \partial x_j + \partial \bar{u}_j / \partial x_i)$ is the resolved strain-rate tensor. The Smagorinsky model [21] is used to model the eddy viscosity where $\nu_T = (C_s \Delta)^2 |\bar{S}|$. In this model, C_s is the Smagorinsky constant, which remains to be determined, and Δ is a measure of the local grid spacing.

The key to closing this system of equations then is to obtain an appropriate value of the Smagorinsky constant C_s . Here the spanwise-averaged version of the dynamic model [17,22] is used for the parametrization of the subgrid scale stresses. In the dynamic model [17] a procedure is used that allows for the estimation of the Smagorinsky constant from the instantaneous resolved flow. Further details of this model are available in the references mentioned above. However, it is important to note that this model has a number of features that make it attractive for complex transitional and turbulent flow. These include (a) no *ad hoc* specification of model constants; (b) no requirement for a wall model; (c) automatic detection of laminar and turbulent regions; and (d) capability to predict transition to turbulence [23]. The last two are especially attractive for pulsatile arterial flows since, first, these flows constantly cycle between laminar and turbulent states, and second, a capability for *predicting* the onset of turbulence obviates the need for any *ad hoc* assumptions regarding the transition process.

Spatial and Temporal Discretization. The three-dimensional governing equations, Eq. (1), are cast in a generalized curvilinear coordinate system in the $(x_1 - x_2)$ plane whereas the x_3 direction

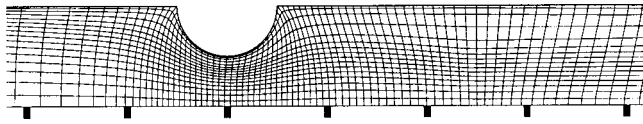


Fig. 2 Two-dimensional view of the mesh in the vicinity of the stenosis. Only every second grid point in the x_1 and every fourth point in the x_2 direction is shown.

is retained as a planar direction. A fully staggered arrangement of the primitive variables is used in the (x_1-x_2) plane and the equations are written in terms of the velocity fluxes on the cell faces. The spatial discretization scheme is a mixed finite-difference-spectral scheme where a second-order central difference scheme is used in the (x_1-x_2) plane and a Fourier spectral method is used in the spanwise (x_3) direction. A two-dimensional view of the mesh in the vicinity of the stenosis is shown in Fig. 2.

A fractional-step scheme [24] is used for advancing the solution in time. In this scheme the equations are advanced first to an intermediate step, where only the convection and diffusion effects are taken into account. This is followed by the pressure correction step, which requires the solution of the Poisson equation for pressure. Subsequently the pressure correction is added to the intermediate velocity field, thereby resulting in a divergence free final velocity. A mixed implicit-explicit scheme is used for the advection-diffusion equation wherein a third-order Runge-Kutta scheme is used for the nonlinear convection and cross terms and a Crank-Nicolson scheme is used for the diagonal viscous terms. This discretization scheme avoids the viscous stability constraints, which can be quite restrictive for these types of computations.

Results and Discussion

Large-eddy simulation has been carried out for the described geometry with $Re=2000$ and $St_0=0.024$, which corresponds to a Womersley number of about 8.7. The spanwise domain size is chosen equal to the channel height and all the results presented here have been obtained on a $240 \times 64 \times 16(x_1 \times x_2 \times x_3)$ grid, which corresponds to about a quarter million mesh points. The grid is nonuniform in the x_1 and x_2 directions with enhanced resolution in the post-stenotic region and in the wall boundary layers. A small random spanwise disturbance is provided at the beginning of the simulation and subsequently the three dimensionality is allowed to develop on its own through the inherent instability of the flow. Eventually the flow reaches a stationary state and the simulation is carried beyond this for about eight cycles and statistics accumulated over this period. The simulation has been carried out on a 195 MHz SGI Origin-2000 multiprocessor computer. Each cycle takes about 37 CPU hours on one node and the entire simulation takes about 500 CPU hours on one node of this computer.

Thin shear layers and boundary layers are formed in this flow that induce large gradients in the vertical direction. Thus, demonstrating the adequacy of the grid in this direction is crucial. One additional simulation has been carried out on a $240 \times 96 \times 16(x_1 \times x_2 \times x_3)$ mesh, which contains 50 percent more points in the vertical direction than the previous mesh. This simulation requires about 55 CPU hours per cycle. In order to reduce the total computation time for this simulation, the solution from the $240 \times 64 \times 16$ mesh has been used to initiate this simulation. Furthermore, this simulation is run for fewer cycles, which is just adequate for accumulating converged first-order statistics like the mean velocity. In Fig. 3 are plotted the mean velocity profiles in the vicinity of the stenosis as obtained from these two simulations. These have been computed by averaging over time as well as the homogeneous spanwise direction. The profiles from the two simulations are found to be in good agreement with each other, with maximum differences being less than 5 percent of U , where $U = Q_{max}/H$ is the characteristic velocity for this flow. This clearly indicates that

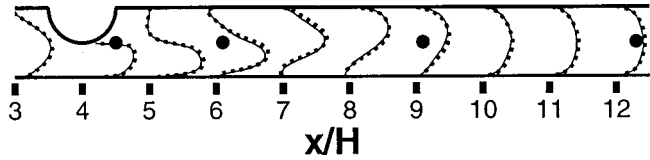


Fig. 3 Comparison of mean velocity profiles obtained from two different simulations. The solid and dotted lines correspond to $240 \times 64 \times 16$ and $240 \times 96 \times 16$ meshes, respectively. The solid circles indicate locations where temporal variation of flow variable is extracted for frequency analysis.

the 64 points used in the vertical direction provide adequate accuracy in the current simulation. With some measure of confidence in the computed results, the focus now shifts to describing the results of the LES. All results presented here have been obtained on the $240 \times 64 \times 16$ mesh and furthermore, have been extracted after the flow has reached a stationary state.

Figure 4 shows a sequence of four plots of the spanwise-averaged spanwise vorticity. Spanwise vorticity is denoted by ω_z and is equal to $(\partial u_2 / \partial x_1 - \partial u_1 / \partial x_2)$. Figure 4(a) corresponds to the phase in the cycle where the inlet volume flux is zero ($t/T=0$) and the spanwise vorticity contours show the remnants of the vortical structures formed downstream of the stenosis in the previous cycle. Figure 4(b) corresponds to the phase in the cycle where the volume flux is half its maximum value and the flow has maximum acceleration ($t/T=0.25$). It can be seen from the figure that the rapidly increasing velocity results in the creation of a shear layer at the lip of the stenosis. This shear layer separates and begins to roll up into a counterclockwise rotating vortex. Furthermore, the increasing velocity in the stenosis region also induces a relatively intense vorticity layer on the bottom wall, which is induced to separate and lift up from the bottom wall by the action of the counterclockwise vortex. Figure 4(c) corresponds to the phase of maximum volume flux ($t/T=0.50$) and the vorticity plot shows an extremely complex flow field. It can be observed that the flow field is dominated by a number of large vortices. The shear layer that separates from the lip of the stenosis rolls up periodically into vortices, which are shed and then travel downstream. In fact, the vortex seen developing in Fig. 4(b) has already traveled downstream and is now located near the upper wall at about $x/H=10$. In addition to the vortices that develop from the separated shear layer, the vorticity layer on the lower wall also rolls up into

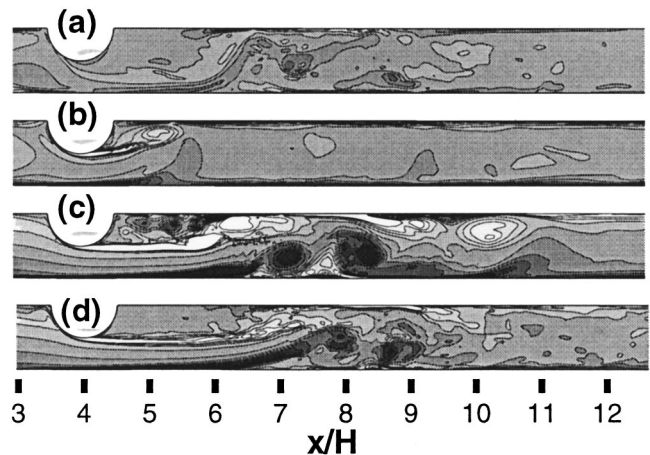


Fig. 4 Sequence of four spanwise-averaged, spanwise vorticity plots over one flow cycle for the $Re=2000$, $St_0=0.024$ case. Dark and light shades represent clockwise and counterclockwise vorticity, respectively. (a) $t/T=0$, (b) $t/T=0.25$, (c) $t/T=0.5$, (d) $t/T=0.75$.

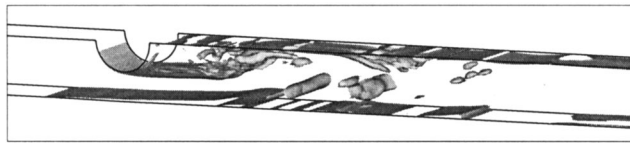


Fig. 5 Three-dimensional isosurface plot of spanwise vorticity corresponding to Fig. 4(c)

large clockwise rotating vortices, which interact with the shear layer vortices as they travel downstream. Finally, Fig. 4(d) corresponds to the phase in the cycle when the mass flux is half the maximum value and the flow has maximum deceleration ($t/T = 0.75$). The effect of the deceleration is to inhibit the rollup of the shear layer and as a result the shear layer extends far downstream at this time instant.

It is worthwhile pointing out that these spanwise-averaged plots do not give a full appreciation of the three-dimensional structure of the flow. This is seen best by looking at the three-dimensional variation of spanwise vorticity. In Fig. 5 is shown an iso-surface plot of spanwise vorticity corresponding to Fig. 4(c). From this figure it is clear that the shear layers that develop on the stenosis and the lower wall are primarily two dimensional but become three dimensional downstream where the vortex rollup occurs.

In Fig. 6, the mean velocity and pressure fields are shown. These mean quantities have been computed by averaging over a number of cycles as well as the homogeneous spanwise direction. Figure 6(a) shows a streamline plot corresponding to the mean velocity field. The plot shows a large mean recirculation zone behind the stenosis on the upper wall, which extends about $3H$ downstream of the stenosis. In addition to this, there also exists a smaller recirculation zone on the lower wall. Figure 6(b) shows a gray-scale contour plot of the mean pressure. In this plot dark and light shades correspond to high and low pressures, respectively. As expected, there is a significant pressure drop due to the presence of the stenosis. Furthermore, it is also readily apparent that the recirculation regions observed in Fig. 6(a) are associated with regions of low pressure.

As mentioned earlier, it has been hypothesized that the distribution and magnitude of the shear stress and pressure on the arterial walls play a role in the genesis and acceleration of arterial diseases. For instance, local hypertension may be directly caused by localized increase in lateral wall pressure [25]. It has also been established that sites of predilection for atherosclerosis are often correlated with regions of low shear stress [26,27]. On the other hand, high shear stress might also lead to platelet activation [28], which can accelerate atherosclerosis. In Figs. 7(a) and 7(b) are plotted the variation of the skin friction and pressure coefficient on both channel walls. The skin friction and pressure coefficients are defined as $C_f = \tau_w / q_0$ and $C_p = (p - p_0) / q_0$, respectively. Here τ_w is the wall shear, p_0 is the reference mean inlet pressure, and $q_0 = 1/2\rho U^2$. A number of interesting observations can be made from these plots. First, the largest mean shear stress is experienced on the stenosis surface just upstream of the tip of the

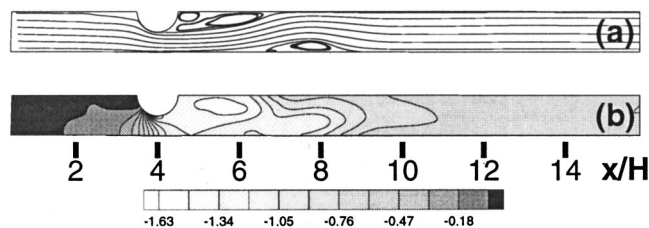


Fig. 6 Mean flow characteristics obtained by averaging in time and along the spanwise direction: (a) streamline plot; (b) contour plot of pressure

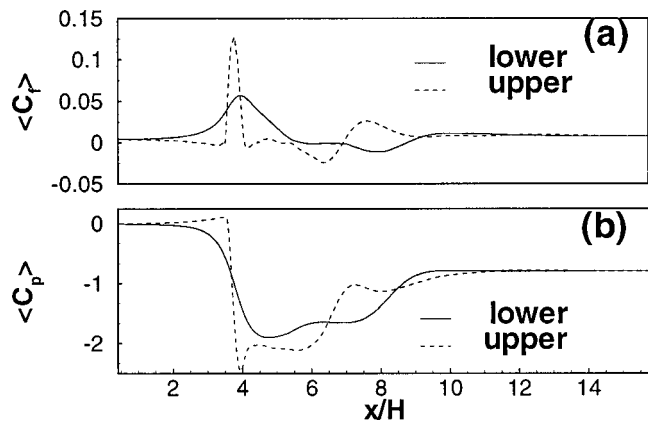


Fig. 7 Nondimensional shear stress and pressure on the lower and upper walls of the channel: (a) skin friction coefficient C_f ; (b) pressure coefficient C_p

stenosis. On the lower wall also, the shear stress reaches a maximum just below the tip of the stenosis. Downstream of the stenosis, the shear stress exhibits local extrema, which are directly related to the mean recirculation regions observed in Fig. 6(a). The mean pressure coefficient plots in Fig. 7(b) also show the significant pressure drop that occurs across the stenosis. On both walls, the pressure drops significantly across the stenosis and then stays at a relatively low value until about $x = 6H$. Beyond this, the pressure increases and attains an almost constant value, which is significantly lower than that at the inlet. The plot indicates that the overall pressure drop between the inlet and exit is $(p_{exit} - p_0) / q_0 = -0.8$.

In addition to the mean pressure and shear stress on the wall, the fluctuation level in these quantities is also of considerable interest. Pressure fluctuations on the arterial wall produces acoustic signals that can be detected externally [7,12]. Furthermore, it has been noted that highly variable wall shear stress can also result in a predilection toward atherosclerosis. The variability in shear stress can prevent endothelial cells from aligning in the direction of the flow, thereby making the intima more permeable to the entry of monocytes and lipoproteins [29,30]. In Fig. 8 the variation of the root-mean-square (rms) skin friction coefficient and pressure gradient on the two walls is plotted. It is convenient and more insightful to plot the rms of the pressure gradient itself, since this automatically de-emphasizes the low-frequency part of the pressure fluctuation associated with the pulsatile flow. It is

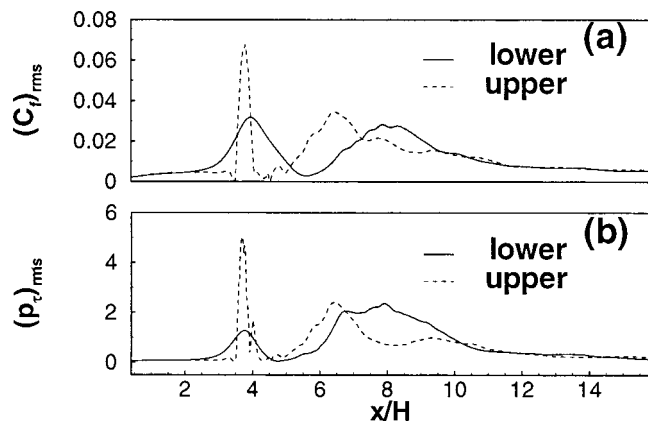


Fig. 8 Root mean square (rms) shear stress and pressure gradient on the lower and upper walls of the channel: (a) root mean square skin friction coefficient $(C_f)_{rms}$; (b) root-mean-square pressure gradient $(p_\tau)_{rms}$

observed that the two sets of plots bear a striking resemblance to each other, which again underscores the direct relationship between the pressure and velocity gradients in the channel. Both plots show a relatively high level of variability in the region of the stenosis. However, interestingly, the plot also indicates a localized region of high shear and pressure gradient fluctuations downstream of the stenosis. On the lower wall, this local maximum is located at about $x/H=8$, and for the upper wall it occurs at about $x/H=6.5$. The high fluctuation level at these particular locations can be traced back to the vortex dynamics of post-stenotic flow. Figure 4(c) clearly shows that vortices from the separated shear layer coming off the stenosis impact the upper wall at about $x/H=6.5$ and this directly causes the large fluctuation in wall pressure and shear stress observed at this location. Similarly, the vorticity layer that separates from the lower wall rolls up into large vortices as observed in Figs. 4(c) and 4(d). These large vortices develop in the region $7 < x/H < 9$ near the lower wall and this causes the large variability in the wall shear and pressure observed in this location.

Additional insight into the dynamics of the flow can be gained by analyzing the temporal variation of the streamwise velocity downstream of the stenosis. In Fig. 9(a) are plotted the variation of the streamwise velocity with time at the channel centerline at four different streamwise locations downstream of the stenosis. The curve marked (i) corresponds to a location of $x/H=4.5$, which lies upstream of the region where the vortex rollup happens. At this location, the velocity variation is mostly sinusoidal except for a small perturbation that appears at about $t/T=0.25$. This perturbation is caused by the passage of the starting vortex, which can be clearly observed in Fig. 4(b). Curve (ii) in Fig. 9(a) shows the temporal variation at $x/H=6.1$, and this figure shows the presence of high-frequency oscillations superposed on the flow pulsations. Careful examination of the flow field indicates that the high-frequency oscillations are caused by periodic shedding of vortices from both vorticity layers. This shedding appears at the phase in the cycle where the velocity is close to the maximum and persists for some time beyond this phase. Similar vortex shedding behavior has been observed in the experimental study of Khalifa and Giddens [31] and Lieber and Giddens [32]. Curve (iii) shows the temporal variation further downstream of the stenosis at $x/H=9.1$. This location is downstream of the position of initial rollup of vortices and lies in the region where the vortices start to break down into smaller scale turbulent structures. It can be observed that the velocity variation does not show the organized high-frequency fluctuations observed at $x/H=6.1$. Instead, large-scale fluctuations, occurring primarily in the deceleration phase of the cycle, are observed. The presence of large-scale fluctuations primarily in the deceleration phase has been observed in experiments before [31] and the current LES clearly picks up this feature of post-stenotic flow. Finally, curve (iv) shows the temporal variation at $x/H=12.3$, which is significantly downstream of the stenosis. Again, it is found that most of the fluctuations appear in the deceleration phase of the cycle. However, comparison with the velocity variation at $x/H=9.1$ clearly shows that the viscosity has significantly attenuated the strength of the turbulent fluctuation.

The frequency of the vortex shedding can be determined by computing the Fourier spectrum of the temporal variations. However, due to the complexity of the shedding process, there is significant cycle-to-cycle phase jitter in the high-frequency fluctuation. Thus, a straightforward Fourier analysis of the entire time trace tends to diminish the peak corresponding to the high-frequency vortex shedding. A phase-averaging technique has therefore been employed that minimizes the effect of the phase jitter and provides an accurate view of the high-frequency part of the spectrum. This type of decomposition in the analysis of fluid flow was first suggested by Reynolds and Hussain [33] and used in the context of pulsatile arterial flows by Khalifa and Giddens [34]. Here a brief description of this technique is provided and the

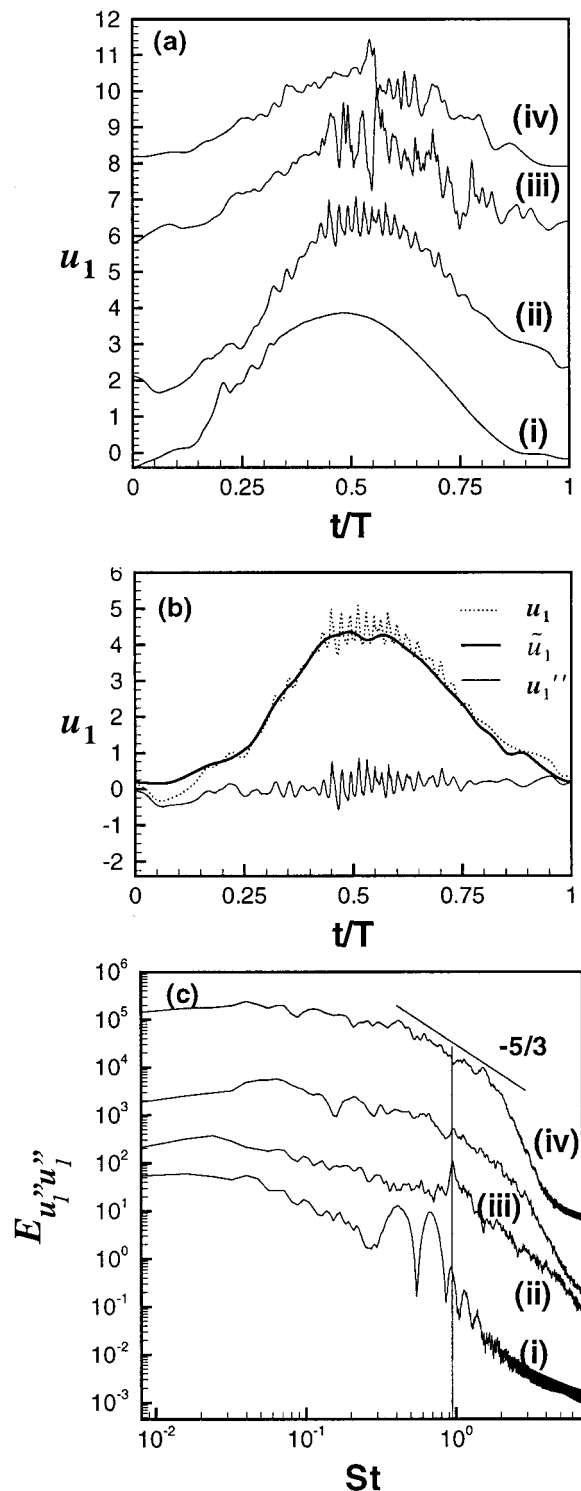


Fig. 9 (a) Temporal variation of streamwise velocity (u_1) over one cycle at various locations on the channel centerline. The locations have been indicated by solid circles in Fig. 3. The plots have been offset in the vertical direction. (i) $x/H=4.5$; offset=0; (ii) $x/H=6.1$; offset=+2; (iii) $x/H=9.1$; offset=+6; (iv) $x/H=12.3$; offset=+8. (b) plot of velocity variation, its phase average (\bar{u}_1) and deviation from phase average (u_1') at $x/H=6.1$. (c) Frequency spectra of (u_1') corresponding to the variations in Fig. 9. The spectra have been offset by a factor in the vertical direction. (i) $x/H=4.5$; offset= $\times 1$; (ii) $x/H=6.1$; offset= $\times 10$; (iii) $x/H=9.1$; offset= $\times 100$; (iv) $x/H=12.3$; offset= $\times 2000$. Vertical line in the spectra indicates the Strouhal number(=0.94) of the high-frequency vortex shedding.

reader is referred to these two papers for further details. In this approach the time variation of a quantity f is decomposed as:

$$f(x,t) = \bar{f}(x_1, x_2, t) + f''(x,t) \quad (2)$$

where \bar{f} is the time-varying coherent (or deterministic or phase-average) part of the flow and is usually computed by ensemble-averaging in experiments [33]. Here this quantity has been computed by phase-averaging over each flow cycle and also along the homogeneous spanwise direction. Deviation away from this phase-average is identified as the incoherent part of the signal and is denoted by f'' . In the temporal analysis of fluid flow data, this decomposition has the advantage that it provides some measure of separation between time scales that are directly the result of the low-frequency forcing and scales that are characteristic of turbulence or other high-frequency phenomena. Figure 9(b) shows the instantaneous variation of the streamwise velocity (u_1) at $x/H = 6.1$ along with its phase average (\bar{u}_1) and the deviation (u_1'') away from the phase average. As can be clearly observed, the phase average comprises primarily of the low-frequency variation, whereas the fluctuation component captures the high-frequency part of the temporal variation.

In Fig. 9(c) the frequency spectra corresponding to the temporal variation of u_1'' has been plotted. At each probe location, the frequency spectrum has been computed and averaged over each cycle as well as over the 16 spanwise locations. The spectrum is presented as a log-log plot, and the spectrum for each probe has been shifted along the ordinate so as to present all the data in the figure. Curve (i) corresponds to the location $x/H = 6.1$. The key difference between this and the previous spectrum (i), which corresponds to the location $x/H = 4.5$, is the presence of a peak at about $St = 0.94$, which corresponds to the high-frequency oscillation observed in Fig. 9(a). Curves (iii) and (iv) correspond to the spectra at $x/H = 9.1$ and 12.3 , respectively. The notable feature here is that the high-frequency peak at $St = 0.94$ is absent and there are no other distinctive peaks in the high-frequency range. Also plotted here is a line with slope corresponding to $(St)^{-5/3}$. By comparing with this line, it is noted that the spectrum at $x/H = 12.3$ does contain a short inertial subrange [35] in the Strouhal number range from 0.4 to 1.4. This suggests that the flow far downstream of the stenosis is turbulent, although the short inertial range points to a flow that is far from being a fully developed equilibrium turbulent flow. As mentioned earlier in the introduction, this is expected to be a characteristic of flows in large arteries.

In Fig. 10(a) the temporal variation of the pressure coefficient over one cycle at four streamwise location on the lower wall has been plotted. The streamwise locations coincide with those in Fig. 9(a). The plot shows that even at the lower wall the pressure clearly shows the signature of the high-frequency fluctuation at $x/H = 6.1$. In fact, the corresponding frequency spectrum of p'' at this location shown in Fig. 10(b) also exhibits a peak at around $St = 0.94$. This has important implications from a diagnostic point of view since it indicates that acoustic signals corresponding to this high-frequency fluctuation have the potential of being transmitted through the arterial wall and may be detectable through noninvasive procedures such as phonoangiography [12].

It should be pointed out that high-frequency vortex formation in separated shear layers is a well-known phenomenon in bluff-body wakes [9,36] where it has been found that the shear layer frequency (f_{SL}) scales as $f_{SL} = 0.0235 f_K Re_d^{0.67}$ where f_K is the Karman vortex shedding frequency and Re_d is the Reynolds number based on the cylinder diameter and free-stream velocity. Given that at high Reynolds numbers, the Strouhal number corresponding to Karman vortex shedding from a circular cylinder is approximately constant at 0.21, this scaling indicates that a shear layer Strouhal number of 0.94 would occur at $Re_d \approx 2520$. This is higher than the maximum inlet Reynolds number in the current simulation. However, the Reynolds number based on the velocity

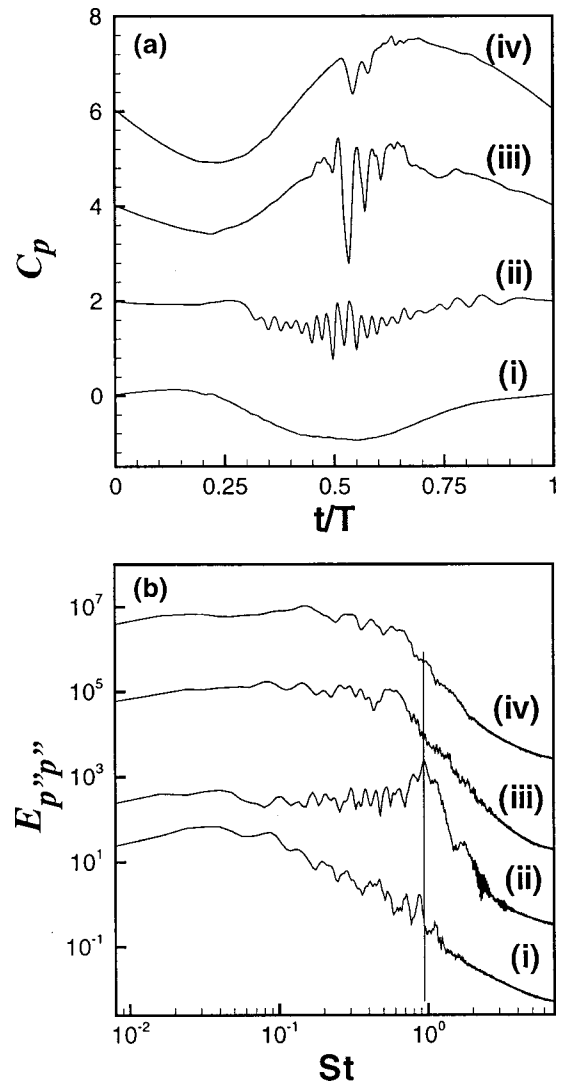


Fig. 10 (a) Temporal variation of pressure coefficient over one cycle at various streamwise locations on the lower wall at streamline locations corresponding to previous plot. The plots have been offset in the vertical direction. (i) $x/H = 4.5$; offset = 0; (ii) $x/H = 6.1$; offset = +4; (iii) $x/H = 9.1$; offset = +8; (iv) $x/H = 12.3$; offset = +12. (b) Frequency spectra of p'' corresponding to the pressure variations in Fig. 10(a). The spectra have been offset by a factor in the vertical direction. (i) $x/H = 4.5$; offset = $\times 1$; (ii) $x/H = 6.1$; offset = $\times 10$; (iii) $x/H = 9.1$; offset = $\times 10^3$; (iv) $x/H = 12.3$; offset = $\times (5 \times 10^5)$. Vertical line in the spectra indicates the Strouhal number ($= 0.94$) of the high-frequency vortex shedding.

in the stenosis is expected to be higher due to the contraction of the channel, and therefore it is quite possible that the high frequency observed in post-stenotic flow could be governed by a scaling relationship similar to that for bluff-body wakes. Obtaining such a correlation between stenotic severity and frequency of pressure fluctuations could prove useful in the diagnosis of arterial disease. Testing of this hypothesis requires a systematic parameter study and a series of simulations is currently being performed in order to examine such a scaling law for post-stenotic flows.

In addition to the mean flow quantities, statistics involving the velocity fluctuations are also important in the physical description of turbulent flows. Quantities such as turbulent stresses and turbulence kinetic energy are dynamically significant, since they quantify the momentum and energy exchange that results from the turbulent fluctuations. Predicting the distribution of these statisti-

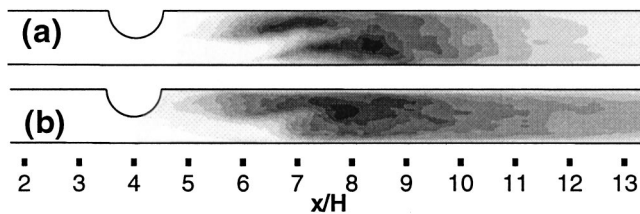


Fig. 11 (a) Contour plot of fluctuation kinetic energy; (b) contour plot of averaged subgrid scale (SGS) viscosity. In both plots, dark shades represents higher magnitudes.

cal quantities is also important from hemodynamic considerations, since blood flowing through regions of high-intensity turbulence would experience high mixing rates and individual blood cells would experience highly variable hydrodynamic forces. In this regard, LES offers a significantly better prediction capability than conventional RANS simulations, where these turbulence quantities are completely modeled and therefore prone to large errors.

In Fig. 11(a) a contour plot of the fluctuation kinetic energy, which is given by the average of $(1/2)(u''_i u''_i)$, has been plotted. It can be seen that the fluctuation kinetic energy computed from the decomposition in Eq. (2) correctly indicates that there are no high-frequency fluctuations upstream of the stenosis. Furthermore, the plot also shows that high-intensity fluctuations are generated in the locations where the two shear layers roll up into vortices. This region of significant fluctuations extends from about $6H$ to $10H$ in the streamwise direction. Beyond this region, the fluctuations decay under the influence of viscosity.

Figure 11(b) shows the time-averaged subgrid-scale (SGS) eddy viscosity, which has been normalized by the molecular viscosity. A number of interesting observations can be made from this plot. The plot clearly shows that the SGS eddy viscosity is virtually zero upstream of the stenosis. This is consistent with the fact that even though the flow upstream of the stenosis is unsteady, it remains laminar. Furthermore, the eddy viscosity is also small in the shear layer separating from the stenosis, and this is also as expected since transition to turbulence is expected to occur in the downstream end of the shear layer. Most of the SGS viscosity is produced in the region where the shear layers roll up into vortices. This is consistent with the observation that the fluctuation kinetic energy also has a large magnitude in this region. Thus the SGS model activated primarily in regions where the flow is turbulent. As pointed out earlier, this is one of the attractive features of the dynamic subgrid scale modeling procedure. The actual magnitude of the SGS eddy viscosity depends on the intensity of turbulence and the grid resolution. In the current simulation the maximum averaged value of the normalized SGS viscosity in this region is about 0.7, which indicates that the SGS component adds up to 70 percent extra viscosity to the flow.

Summary

In this paper the application of the technique of large-eddy simulation to the study of flow in a modeled arterial stenosis is presented. A simple model with a semicircular one-sided stenosis in a planar channel has been chosen. The flow at the channel inlet is varied in a sinusoidal manner, and the peak Reynolds number and Strouhal number of the simulation are 2000 and 0.024, respectively. Despite the simplicity of the geometrical model, the simulated flow exhibits a number of features that match well with experiments that have been carried out in more realistic geometries. In particular, the flow downstream of the stenosis shows all the classic features of post-stenotic flow that have been observed before in the experiments of Khalifa and Giddens [31] and Lieber and Giddens [32]. In addition to this, flow visualizations and frequency spectra also provide additional insight into the evolution of the vortical structures downstream of the stenosis. Flow statis-

tics have been accumulated over a number of flow cycles. This allows us to clearly pinpoint the region where most of the turbulence is generated. It is also shown that the SGS model activates in regions of high turbulence intensity and in the current simulation, the subgrid-scale eddy viscosity contributes up to about 70 percent extra viscosity to the flow. Finally, the current simulations show that the flow immediately downstream of the stenosis is for the most part transitional in nature. However, farther downstream, the spectra indicate the presence of a fully turbulent flow with a short inertial subrange.

In the current study, an attempt has been made to demonstrate that large-eddy simulation is well suited for the simulation and analysis of turbulent and transitional cardiovascular flows. The many unique features of LES lead to its effectiveness and promise in providing information that could prove invaluable in our understanding of complex arterial flows and diagnosis of arterial disease. However, even for the relatively simple flow investigated here, over 500 CPU hours are needed to complete the study. Thus, the wealth of information obtained from LES comes at a significant computational cost; therefore, highly efficient algorithms and state-of-the-art computers need to be used if this technique is to be applied to the study of complex cardiovascular flows. The work presented in this paper is currently being extended to obtain information on the correlation between stenosis degree and post-stenotic flow behavior. Such information could potentially have an impact on the noninvasive diagnosis of arterial disease.

Acknowledgments

These computations have been performed on the SGI-Cray Origin-2000 at the National Center for Supercomputing Applications (NCSA).

References

- [1] Fung, Y. C., 1997, *Biomechanics: Circulation*, 2nd ed., Springer-Verlag, New York.
- [2] Pedley, T. J., 1980, *The Fluid Mechanics of Large Blood Vessels*, Cambridge University Press, Cambridge.
- [3] White, F. M., 1991, *Viscous Fluid Flow*, McGraw-Hill, New York.
- [4] Winter, D. C., and Nerem, R. M., 1984, "Turbulence in Pulsatile Flows," *Ann. Biomed. Eng.*, **12**, pp. 357–369.
- [5] Davies, C., and Carpenter, P. W., 1997, "Numerical Simulation of the Evolution of Tollmien–Schlichting Waves Over Compliant Panels," *J. Fluid Mech.*, **335**, pp. 361–392.
- [6] Ku, D. N., 1997, "Blood Flow in Arteries," *Annu. Rev. Fluid Mech.*, **29**, pp. 399–343; *Arteriosclerosis*, **5**, pp. 289–302.
- [7] Nichols, W. W., and O'Rourke, M. F., 1998, *McDonald's Blood Flow in Arteries Theoretical, Experimental and Clinical Principles* 4th ed., Oxford University Press, New York.
- [8] Roshko, A., 1954, "On the Development of Turbulent Wakes From Vortex Streets," NACA Report 1191, pp. 124–132.
- [9] Bloor, M. S., 1964, "The Transition to Turbulence in the Wake of a Circular Cylinder," *J. Fluid Mech.*, **21**, p. 290.
- [10] Giddens, D. P., Zarins, C. K., and Glagov, S., 1993, "The Role of Fluid Mechanics in the Localization and Detection of Atherosclerosis," *ASME J. Biomech. Eng.*, **115**, pp. 588–594.
- [11] Downing, J. M., and Ku, D. N., 1997, "Effects of Frictional Losses and Pulsatile Flow on the Collapse of Stenotic Arteries," *ASME J. Biomech. Eng.*, **119**, pp. 317–324.
- [12] Lees, X. X., and Dewey, Y. Y., 1970, "Phonoangiography: A New Noninvasive Diagnostic Method for Studying Arterial Disease," *Physica A*, **67**, No. 2, pp. 935–942.
- [13] Cloutier, G., Allard, L., and Durand, L.-G., 1996, "Characterization of Blood Flow Turbulence With Pulsed-Wave and Power Doppler Ultrasound Imaging," *ASME J. Biomech. Eng.*, **118**, pp. 318–325.
- [14] Rogallo, R. S., and Moin, P., 1984, "Numerical Simulation of Turbulent Flows," *Annu. Rev. Fluid Mech.*, **16**, pp. 99–137.
- [15] Wilcox, D. C., 1998, *Turbulence Modeling for CFD*, DCW Industries.
- [16] Tutty, O. R., 1992, "Pulsatile Flow in a Constricted Channel," *ASME J. Biomech. Eng.*, **114**, pp. 50–54.
- [17] Germano, M., Piomelli, U., Moin, P., and Cabot, W., 1991, "A Dynamic Subgrid-Scale Eddy Viscosity Model," *Phys. Fluids*, **A3**, pp. 1760–1765.
- [18] Lesieur, M., and Metais, O., 1994, "New Trends in Large-Eddy Simulation," *Annu. Rev. Fluid Mech.*, **28**, pp. 45–82.
- [19] Mittal, R., and Moin, P., 1997, "Suitability of Upwind-Biased Schemes for Large-Eddy Simulation of Turbulent Flows," *AIAA J.*, **35**, No. 8, pp. 1415–1417.
- [20] Kaltenbach, H.-J., Fatica, M., Mittal, R., Lund, T. S., and Moin, P., 1999,

- “Study of Flow in Planar Asymmetric Diffuser Using Large-Eddy Simulation,” *J. Fluid Mech.*, **390**, pp. 151–186.
- [21] Smagorinsky, J., 1963, “General Circulation Experiments With the Primitive Equations,” *Mon. Weather Rev.*, **91**, No. 3, pp. 99–164.
- [22] Lilly, D. K., 1992, “A Proposed Modification of the Germano Subgrid-Scale Closure,” *Method. Phys. Fluids*, **A4**, pp. 633–635.
- [23] Piomelli, U., 1999, “Large-Eddy Simulation: Achievements and Challenges,” *Prog. Aerosp. Sci.*, **35**, No. 4, pp. 335–362.
- [24] Chorin, A. J., 1968, “Numerical Solution of the Navier–Stokes Equations,” *Math. Comput.*, **22**, pp. 745–757.
- [25] Holman, E., 1955, “The Development of Arterial Aneurysms,” *J. Surgical Gynecology Obstetrics*, **100**, pp. 599–611.
- [26] Ku, D. N., Giddens, D. P., Zarins, C. K., and Glagov, S., 1985, *Pulsatile Flow and Atherosclerosis in the Human Carotid Bifurcation*.
- [27] Friedman, M. H., Hutchins, G. M., Barger, C. B., Deters, O. J., and Mark, F. F., 1981, “Correlation Between Intimal Thickness and Fluid Shear in Human Arteries,” *Atherosclerosis*, **39**, pp. 425–436.
- [28] Stein, P. D., Walburn, F. J., and Sabbah, H. N., 1982, “Turbulent Stresses in the Region of Aortic and Pulmonary Valves,” *ASME J. Biomech. Eng.*, **104**, pp. 238–244.
- [29] Nerem, R. M., 1992, “Vascular Fluid Mechanics, the Arterial Wall and Atherosclerosis,” *ASME J. Biomech. Eng.*, **114**, pp. 274–282.
- [30] Zarins, C. K., and Glagov, S., 1994, “Pathophysiology of Human Atherosclerosis,” in: F. J. Vieth, R. W. Hobson II, R. A. Williams, et al., eds., *Vascular Surgery—Principles and Practice*, 2nd ed., McGraw-Hill, New York, pp. 21–39.
- [31] Khalifa, A. M. A., and Giddens, D. P., 1981, “Characterization and Evolution of Post-Stenotic Flow Disturbances,” *J. Biomech.*, **14**, pp. 279–296.
- [32] Lieber, B. B., and Giddens, D. P., 1990, “Post-stenotic Core Flow Behavior in Pulsatile Flow and Its Effects on Wall Shear Stress,” *J. Biomech.*, **23**, No. 6, pp. 597–605.
- [33] Reynolds, W. C., and Hussain, A. K. M. F., 1972, “The Mechanics of an Organized Wave in Turbulent Shear Flow. Part 3. Theoretical Models and Comparisons With Experiments,” *J. Fluid Mech.*, **54**, pp. 263–288.
- [34] Khalifa, A. M. A., and Giddens, D. P., 1978, “Analysis of Disorder in Pulsatile Flows With Applications to Poststenotic Blood Velocity Measurements in Dogs,” *J. Biomech.*, **11**, pp. 129–141.
- [35] Tennekes, H., and Lumley, J. L., 1972, *A First Course in Turbulence*, MIT Press, Cambridge, MA.
- [36] Prasad, A., and Williamson, C. H. K., 1996, “The Instability of the Separated Shear Layer From a Bluff Body,” *Phys. Fluids*, **8**, No. 6 pp. 1347–1349.